A collective scattering system for measuring electron gyroscale fluctuations on the National Spherical Torus Experiment

D. R. Smith,[1,a)] E. Mazzucato,[1] W. Lee,[2] H. K. Park,[2] C. W. Domier,[3] and N. C. Luhmann, Jr.[3]
[1]*Princeton Plasma Physics Laboratory, Princeton, New Jersey 08543-0451, USA*
[2]*Department of Physics, POSTECH, Pohang 790-784, Republic of Korea*
[3]*Department of Applied Science, University of California at Davis, Davis, California 95616-8254, USA*

(Received 24 July 2008; accepted 9 November 2008; published online 5 December 2008)

A collective scattering system has been installed on the National Spherical Torus Experiment (NSTX) to measure electron gyroscale fluctuations in NSTX plasmas. The system measures fluctuations with $k_\perp \rho_e \lesssim 0.6$ and $k_\perp \lesssim 20$ cm^{-1}. Up to five distinct wavenumbers are measured simultaneously, and the large toroidal curvature of NSTX plasmas provides enhanced spatial localization. Steerable optics can position the scattering volume throughout the plasma from the magnetic axis to the outboard edge. Initial measurements indicate rich turbulent dynamics on the electron gyroscale. The system will be a valuable tool for investigating the connection between electron temperature gradient turbulence and electron thermal transport in NSTX plasmas. © *2008 American Institute of Physics.* [DOI: 10.1063/1.3039415]

I. INTRODUCTION

Transport processes impact the feasibility of magnetic fusion energy by setting the plasma size needed to attain fusion-relevant conditions.[1–3] Plasma turbulence typically drives transport in excess of neoclassical transport, the irreducible minimum transport set by particle collisions. Understanding and reducing turbulent transport presents a grand challenge for fusion energy sciences, and validating turbulence and transport models is critical for extrapolating to next-generation experiments.

Fusion products preferentially heat electrons in burning plasma, but electron thermal transport is generally the most anomalous and least understood transport process. Recent gyrokinetic simulations predict that electron temperature gradient (ETG) turbulence can drive substantial electron thermal transport.[4–9] ETG turbulence occurs on the electron gyroscale with $k_\perp \rho_e \lesssim 1$, where $k_\perp$ is the fluctuation wavenumber perpendicular to the magnetic field and ρ_e is the electron gyroradius. Fluctuation measurements on the electron gyroscale are needed to assess the existence and characteristics of ETG turbulence and ETG-driven electron thermal transport.

The National Spherical Torus Experiment[10,11] (NSTX) is a low-aspect-ratio device, and NSTX plasmas exhibit turbulence and transport properties unlike conventional tokamak plasmas. Most significantly, NSTX high-confinement (H-mode) plasmas routinely exhibit ion thermal transport at or near the neoclassical level. Evidence suggests that large equilibrium $E \times B$ flow shear reduces or suppresses ion gyroscale turbulence, such as ion temperature gradient (ITG) turbulence and trapped electron mode (TEM) turbulence, to enable neoclassical ion thermal transport.[12–17] Electron thermal transport, in contrast, remains anomalous for all NSTX confinement regimes, and ETG turbulence can be linearly unstable in NSTX plasmas. Consequently, NSTX plasmas are well suited for investigating anomalous electron thermal transport and ETG turbulence without complications from ITG/TEM turbulence. To that end, a collective scattering system[18,19] has been installed on NSTX to measure electron gyroscale fluctuations. Collective scattering is a powerful diagnostic technique for measuring density fluctuations with spatial and k-space localization. The NSTX scattering system exploits the large toroidal curvature of NSTX plasmas to achieve enhanced spatial localization.[20,21] This paper describes the capabilities and design of the NSTX scattering system. Principles of collective scattering are reviewed in Sec. II. The NSTX scattering system is described in Sec. III, and initial measurements are presented in Sec. IV. Finally, a summary is given in Sec. V.

II. PRINCIPLES OF COLLECTIVE SCATTERING

Collective scattering measurements provided the first confirmation of core turbulence in tokamak plasmas.[22] Collective scattering amounts to refractive index fluctuations that distort the phase front of an incident electromagnetic wave.[23,24] The distortions propagate as scattered electromagnetic waves, and properties of the scattered waves correspond to properties of plasma fluctuations. Only collective electron motion on scales larger than the Debye length, λ_D, can generate coherent scattered waves so collective scattering measurements must satisfy $k\lambda_D \lesssim 1$, where k is the fluctuation wavenumber.

The dispersion relation for electromagnetic plasma waves at frequencies well above the electron cyclotron frequency is $n_r^2 = 1 - \omega_p^2/\omega^2$, where n_r is the refractive index, ω is the wave frequency, $\omega_p^2 \equiv n_e e^2/\epsilon_0 m_e$ is the plasma frequency, and n_e is the electron density. The susceptibility is $\chi \equiv n_r^2 - 1$. Consider plasma with electron density $n_e(\mathbf{r},t)$ and

a)Electronic mail: drsmith@pppl.gov.

incident and scattered electromagnetic plasma waves with wave vectors $\boldsymbol{k_i}$ and $\boldsymbol{k_s}$, frequencies ω_i and ω_s, and polarizations $\boldsymbol{e_i}$ and $\boldsymbol{e_s}$, respectively. Briefly stated, the frequency spectrum and angular distribution of scattered light reveal the density fluctuation spectrum, $|n_e(\boldsymbol{k},\omega)|^2$, within the scattering volume. The time-averaged scattered power per unit solid angle in the direction $\hat{\boldsymbol{r}} \equiv \boldsymbol{k_s}/k_s$ is

$$\frac{dP_s(\hat{\boldsymbol{r}},t)}{d\Omega} = \frac{P_i}{A}\left(\frac{k_s^2}{4\pi}\boldsymbol{e_i}\cdot\boldsymbol{e_s}\right)^2 \left|\int_V \chi(\boldsymbol{x},t)e^{i\boldsymbol{k}\cdot\boldsymbol{x}}d^3x\right|^2 \tag{1}$$

$$= P_i\frac{r_e^2}{A}(\boldsymbol{e_i}\cdot\boldsymbol{e_s})^2|n_e(\boldsymbol{k},t)|^2, \tag{2}$$

where

$$\boldsymbol{k} \equiv \boldsymbol{k_s} - \boldsymbol{k_i} \tag{3}$$

is the fluctuation wave vector, V is the scattering volume, P_i is the incident power, A is the incident beam cross-sectional area, and $r_e \equiv e^2/4\pi\epsilon_0 m_e c^2$ is the classical electron radius. $P_s(\hat{\boldsymbol{r}},t)$ is averaged over time scales long relative to $1/\omega_s$ and short relative to fluctuations of interest. The time-averaged scattered power per unit solid angle per unit frequency is

$$\frac{d^2P_s(\hat{\boldsymbol{r}},\omega)}{d\Omega d\omega/2\pi} = P_i r_e^2 L(\boldsymbol{e_i}\cdot\boldsymbol{e_s})^2 S(\boldsymbol{k},\omega), \tag{4}$$

where

$$S(\boldsymbol{k},\omega) \equiv \frac{|n_e(\boldsymbol{k},\omega)|^2}{VT} \tag{5}$$

is the density power spectrum, T is the observation time, and $L \equiv V/A$ is the length of the scattering volume along the probe beam. The fluctuation frequency, ω, is a signed quantity, and fluctuations with $\omega < 0$ propagate in the direction $-\boldsymbol{k}$. For a single, coherent density fluctuation with amplitude $\tilde{n}_e$, the total scattered power observed by a receiver with angular aperture $\pi(2/k_i a)^2$ is

$$P_s = \tfrac{1}{4}P_i r_e^2 L^2 \lambda_i^2 \tilde{n}_e^2, \tag{6}$$

where $\lambda_i = 2\pi/k_i$ is the probe beam wavelength.

The scattered wave frequency spectrum is simply the fluctuation frequency spectrum upshifted to the incident wave frequency, so frequencies satisfy $\omega_s = \omega_i + \omega$. Fluctuations are low frequency such that $\omega \ll \omega_i \simeq \omega_s$, so the isotropic dispersion relation gives $k_i \simeq k_s$. Consequently, Eq. (3) represents a geometrical isosceles triangle that satisfies the Bragg condition

$$k = 2k_i \sin(\theta_s/2), \tag{7}$$

where θ_s is the scattering angle between $\boldsymbol{k_i}$ and $\boldsymbol{k_s}$. A receiver at a particular scattering angle is preferentially sensitive to fluctuations that satisfy Eq. (7), and an angular array of receivers can probe the fluctuation k-spectrum at distinct wavenumbers.

The scattering volume and k-space resolution are interconnected. Consider a nondiverging beam with transverse spatial profile $\exp(-r_t^2/a^2)$, where a is the beam radius and r_t is the transverse coordinate. The transverse wavenumber spectrum is $\exp(-k_t^2/\Delta k^2)$, where k_t is the transverse wavenumber coordinate and $\Delta k \equiv 2/a$ is the transverse k-space resolution. For probe and receiving beams with radius a and for small to moderate scattering angles, $\boldsymbol{k}$ is nearly transverse to both $\boldsymbol{k_i}$ and $\boldsymbol{k_s}$ so the k-space resolution for $\boldsymbol{k}$ is approximately Δk.

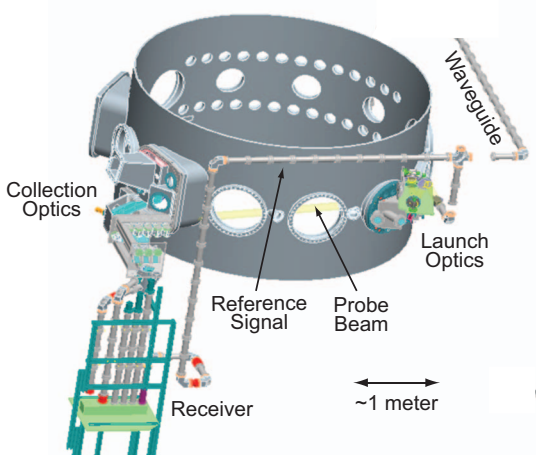

FIG. 1. (Color) Arrangement of the NSTX collective scattering system.

Along the probe beam, the length of the overlap volume is $L_{ol} \simeq 2a/\sin\theta_s$, but the scattering volume length, L_{sv}, can be substantially less due to turbulence anisotropy and magnetic field inhomogeneity. The perpendicular scale of ETG turbulence satisfies $k_\perp \rho_e \lesssim 1$, but the component of $\boldsymbol{k}$ parallel to the magnetic field, $k_\parallel$, satisfies $k_\parallel L_c \sim 1$, where $L_c \equiv qR$ is the connection length. ETG turbulence, therefore, is anisotropic with[7]

$$k_\parallel \ll k_\perp. \tag{8}$$

$\boldsymbol{k}$ is set by Eq. (3), but the components $k_\perp$ and $k_\parallel$ may change within the overlap volume due to magnetic field inhomogeneity such as magnetic shear or curvature. As described in Refs. 20 and 21, the scattering volume is the portion of the overlap volume that satisfies Eqs. (7) and (8). Scattering volume constriction is more pronounced in devices with larger toroidal curvature or larger magnetic shear, so spherical torus devices like NSTX can exploit the effect more than conventional tokamaks.

III. THE NSTX SCATTERING SYSTEM

A. Overview

The NSTX collective scattering system measures density fluctuations with $k_\perp \rho_e \lesssim 0.6$ and $k_\perp \lesssim 20$ cm^{-1}. With five detection channels, the system measures up to five distinct wavenumbers simultaneously with resolution $\Delta k \simeq 0.7$ cm^{-1}. The large toroidal curvature of NSTX plasmas provides enhanced spatial localization along the probe beam with $L \approx 5-15$ cm. Probe and receiving beams lie nearly on the equatorial midplane such that measured fluctuations are primarily radial. Steerable optics can position the scattering volume from the magnetic axis to the outboard edge. High-power microwave source and low-noise detection system enable sensitive fluctuation measurements. Figure 1 shows a schematic of the scattering system, and Fig. 2 shows inboard and outboard measurement configurations.

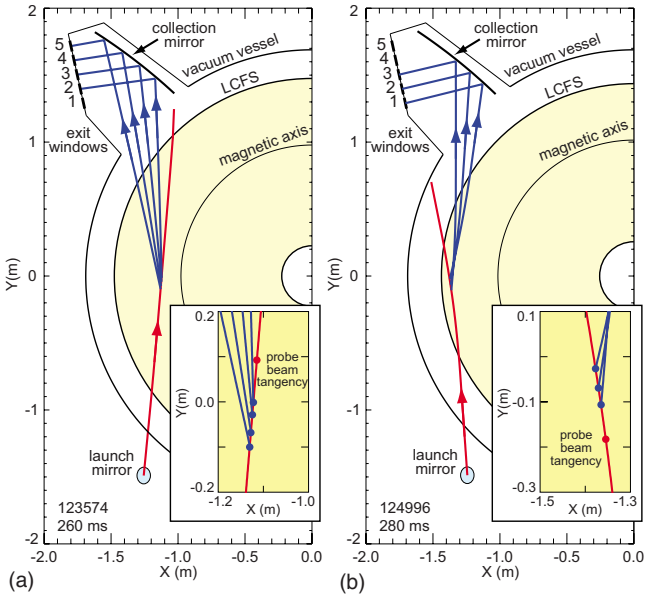

FIG. 2. (Color online) Overhead plots of beam central rays for inboard (a) and outboard (b) measurement configurations are shown. Insets show that receiving beams do not intersect the probe beam tangency as required for k-space alignment.

B. Launch hardware

A backward-wave oscillator (BWO) provides about 150 mW of microwave power at 280 GHz and $\lambda = 1.1$ mm (Thomson-CSF TH-4224S). Overmoded, corrugated waveguide with a 6.3 cm inner diameter transmits microwave power with less than ~3 dB loss as measured by a thermopile detector. The probe beam begins free-space propagation at the waveguide termination outside the vacuum vessel, and the probe beam power is about 100 mW. A series of ex-vessel mirrors directs the probe beam through a water-free quartz window and into the vacuum vessel. An in-vessel steering mirror steers the probe beam horizontally and vertically. The probe beam can access tangency radii from the magnetic axis to the outboard edge near the midplane. Two feedthrough actuators rotate the steering mirror around two axes of rotation to set the mirror orientation.

C. Quasioptical design

As shown in Fig. 3, the probe beam waist at the waveguide termination is 1.6 cm (all beam sizes refer to the $1/e^2$ intensity radius). An ex-vessel focusing mirror (1.5 m focal length) focuses the probe beam to position a 3 cm beam waist at the scattering region in vessel. The corresponding k-space resolution is $\Delta k \simeq 0.7\ \mathrm{cm}^{-1}$.

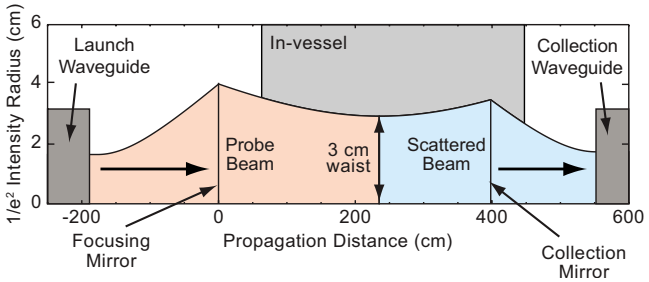

FIG. 3. (Color online) The beam profile is shown as the beam propagates from the launch waveguide outside the vacuum vessel to the scattering region in vessel and finally to the collection waveguide.

D. Collection hardware

Scattering occurs along the entire probe beam, but a fixed observation point observes scattered light only from the probe beam region that satisfies Eqs. (7) and (8). Therefore, a receiver must be properly aligned to observe scattered light. For the NSTX scattering system, scattered light first encounters a large in-vessel collection mirror with a 4.25 m radius of curvature. The collection mirror directs scattered light to five water-free quartz exit windows and focuses scattered light for coupling into collection waveguide segments located outside the vacuum vessel. The horizontal orientation of the collection mirror is adjustable, and a feedthrough actuator controls the orientation. The vertical orientation of the collection mirror is fixed. Steerable exit window mirrors are located outside the vacuum vessel and adjacent to the exit windows. The exit mirrors control the view of the collection waveguide segments through the exit windows into the vacuum vessel. Scattered light does not necessarily arrive at exit windows with normal incidence, so exit mirrors adjust waveguide views to coincide with scattered light from the scattering volume. Rotation stages steer the exit mirrors horizontally, and thumb-screw actuators steer the exit mirrors vertically. When the exit window mirrors are properly aligned, the mirrors direct scattered light into collection waveguide segments.

E. Ray tracing

Ray tracing calculations are needed to configure the scattering system before experiments and to interpret measurements after experiments. The calculations determine refracted beam paths, k-space parameters, Doppler shifts from plasma rotation, and scattering volume lengths. Refraction can deflect beam paths over 10° for measurements in an H-mode edge. The deflection impacts k-space alignment and, to a lesser extent, the measurement radial location. Measured wave vectors typically have a toroidal component, so toroidal rotation from neutral beam injection (NBI) introduces a Doppler shift in the measured spectrum. The natural mode frequency of turbulent fluctuations is generally not known *a priori*, so measured spectra cannot provide rotation measurements. The Doppler shift is calculated from toroidal rotation measurements from the NSTX charge-exchange spectroscopy system.[25] Ray tracing calculations also provide k-space parameters needed to assess k-space alignment and for comparing measurements to turbulence simulations. The component $k_{\|}$ should satisfy Eq. (8) within the k-space resolution, Δk. In the plane perpendicular to the magnetic field, the fluctuation wave vector can be decomposed into radial and binormal components, k_r and k_{bi}, respectively. k_r is the component perpendicular to the flux surface, and k_{bi} is the component perpendicular to $\boldsymbol{B}$ within the flux surface such that $k_{\mathrm{bi}} > 0$ is in the ion diamagnetic drift direction. Fluctuations with $k_{\mathrm{bi}} > 0$ correspond to ion modes, such as the ITG mode, and fluctuations with $k_{\mathrm{bi}} < 0$ correspond to electron modes,

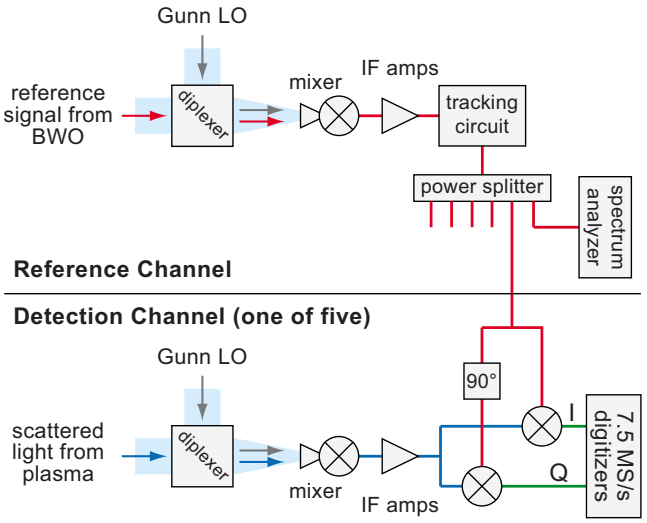

FIG. 4. (Color online) The heterodyne receiver employs two mixing stages and quadrature detection.

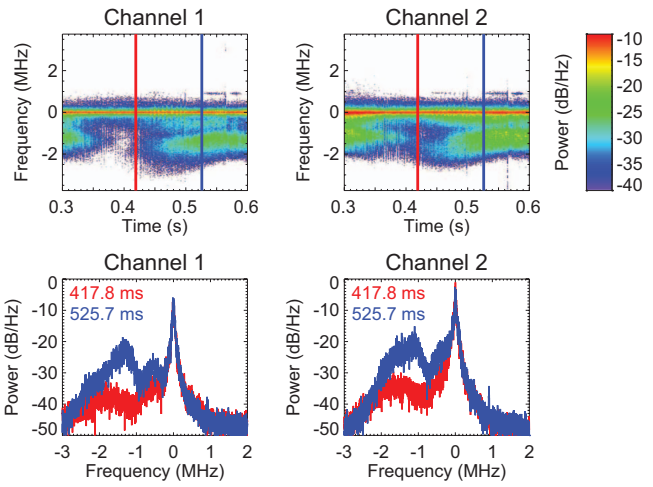

FIG. 5. (Color) Measurements at $r/a \simeq 0.55$ are shown. The system configuration is shown in Fig. 6, and measurement parameters are listed in Table I.

such as the TEM and ETG modes. The components k_r and k_{bi} are needed to compare measured fluctuations to nonlinear gyrokinetic simulations. Finally, ray tracing calculations give the instrument selectivity function and the length of the scattering volume along the probe beam in accordance with Refs. 20 and 21.

F. Heterodyne receiver

A five-channel heterodyne receiver, depicted in Fig. 4, detects scattered light with high sensitivity and low noise. The system employs quadrature detection to preserve phase information to distinguish between fluctuations with wave vectors $+\boldsymbol{k}$ and $-\boldsymbol{k}$. Fluctuations with wave vector $+\boldsymbol{k}$ upshift the frequency of scattered light and fluctuations with wave vector $-\boldsymbol{k}$ downshift the frequency of scattered light. A Gunn oscillator provides the local oscillator (LO) signal, and the BWO frequency is offset from the Gunn frequency by 880 MHz, the intermediate frequency (IF). At the receiver front end, a Michelson diplexer combines scattered light and a LO signal. The combined signals are focused into a fundamental Schottky diode mixer that downconverts scattered light from the 280 GHz BWO frequency to the IF. After mixing, a preamplifier (MITEQ AFS2-008001) provides 31 dB of gain, and an amplifier (Mini-Circuits ZKL-1R5) provides 36 dB of gain. The IF scattered signal is then mixed with an IF reference signal. A small BWO signal and an additional Gunn LO signal are mixed to produce the IF reference signal. The IF reference signal drives a tracking circuit that generates a high-power IF reference signal phase locked with the original IF reference signal. The high-power IF reference signal is split into multiple signals for the second mixing stage, and the IF is monitored with a spectrum analyzer. An inphase-quadrature (I/Q) demodulator (Mini-Circuits ZAMIQ-895D) mixes the IF scattered signal and an IF reference signal, thus downconverting the scattered signal to 0 Hz. The I/Q signals are amplified by video amplifiers and digitized at 7.5 MS/s with 14 bit resolution (D-tAcq ACQ216CPCI). The inphase and quadrature time series, $I(t)$ and $Q(t)$, respectively, constitute the raw data for a single detection channel. The receiver noise power is $P_n = k_B T_n B$, where k_B is the Boltzmann constant, B is the noise bandwidth, and T_n is the receiver noise temperature. The receiver noise power sets the minimum detectable fluctuation. Thermal measurements of receiver noise give noise temperatures in the range of 4500–6000 K among the five detection channels. The front-end mixers do not filter the image signal so the noise bandwidth is 15 MHz. Assuming a noise temperature of 5000 K, the noise power is 10^{-12} W. Equating the noise power to the scattered power in Eq. (6) provides an estimate for the minimum detectable fluctuation. With $P_i = 100$ mW, $L = 10$ cm, and $\bar{n}_e = 5 \times 10^{13}$ cm^{-3}, the minimum detectable fluctuation is $\tilde{n}_e/\bar{n}_e \simeq 4 \times 10^{-6}$. The bremsstrahlung emission at $\omega_i/2\pi = 280$ GHz and $T_e = 1$ keV can be estimated using the low-frequency Born approximation.[26] Using $n_i = \bar{n}_e$ from above, $Z_{\mathrm{eff}} = 1$, the 15 MHz noise bandwidth, and a 1 m plasma column with radius $a = 3$ cm, the bremsstrahlung power is $P_{\mathrm{brem}} \approx 10^{-13}$ W, so bremsstrahlung emission is slightly less than the minimum detectable scattered power.

IV. INITIAL MEASUREMENTS

Measurements for the NSTX discharge 124888 at $r/a \simeq 0.55$ are shown in Fig. 5, the system configuration is shown in Fig. 6, and measurement parameters are listed in Table I. Quadrature detection preserves phase information so frequency is a signed quantity. The ubiquitous peak at zero frequency corresponds to spurious reflections of the probe beam. In Fig. 5, positive frequency corresponds to fluctuation wave vectors with a component in the electron diamagnetic direction, but toroidal rotation Doppler shifts the spectrum to negative frequency (ion diamagnetic direction). The Doppler shift always acts in the ion diamagnetic direction due to the orientation of the high-k system relative to the neutral beam. The Doppler shift during NBI can exceed the natural mode frequency of fluctuations thereby shifting modes that propagate in the electron drift direction in the plasma frame to the ion drift direction in measured spectra, as evident in Fig. 5. The measured spectra demonstrate the existence of electron gyroscale fluctuations in NSTX

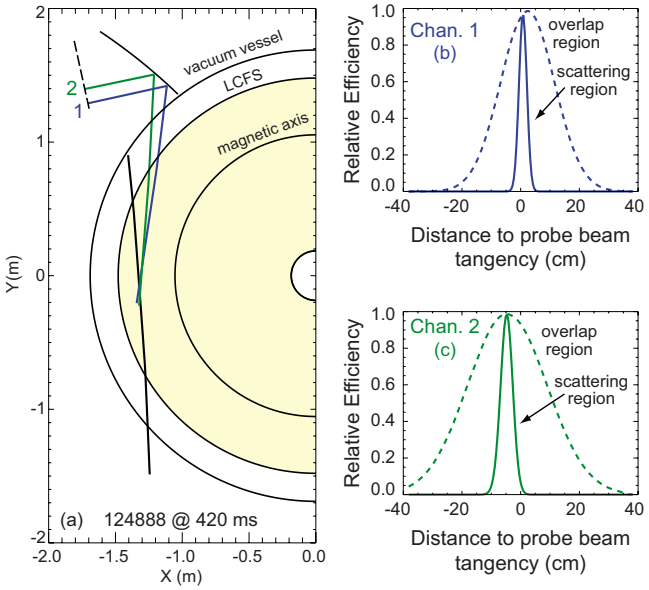

FIG. 6. (Color online) Plot (a) shows the system configuration for data in Fig. 5. Plots (b) and (c) illustrate the length of the scattering volume along the probe beam. Dashed lines are beam overlap regions and solid lines are scattering volume regions.

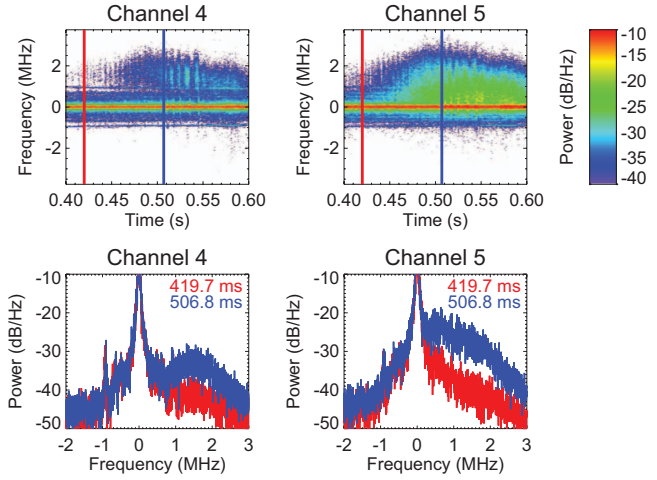

FIG. 7. (Color) Core measurements at $r/a \simeq 0.15$ are shown. Channel 4 corresponds to fluctuations with $k_\perp \rho_e \simeq 0.29$, and channel 5 corresponds to $k_\perp \rho_e \simeq 0.37$.

plasmas. Additionally, the measurements indicate that the nonlinear saturation dynamics evolve with plasma conditions.

Power spectra in Fig. 5 are calculated from fast Fourier transforms (FFTs) of the complex-valued time series $V(t) = I(t) + iQ(t)$. FFTs are calculated with 4096 samples corresponding to 0.55 ms time windows and 1.8 kHz resolution. The Hann window function is applied to FFT windows to improve the dynamic range, and successive windows overlap by half. Finally, spectra are smoothed to enhance readability.

Parts (b) and (c) in Fig. 6 illustrate scattering volume constriction due to turbulence anisotropy and magnetic field inhomogeneity. The large toroidal curvature of the plasma detunes the k-space alignment within portions of the overlap volume to shorten the scattering volume relative to the overlap volume.

TABLE I. Measurement parameters for the data in Fig. 5 are listed. Measurement parameters are obtained from ray tracing calculations.

	Channel 1		Channel 2	
	420 ms	520 ms	420 ms	520 ms
R (cm)	133.2	133.5	133.2	133.4
r/a	0.55	0.57	0.55	0.57
θ_s (deg)	13.0	13.7	8.8	9.6
$k_\perp \rho_e$	0.30	0.29	0.21	0.21
$k_\perp \rho_s$	18.2	17.7	12.5	12.5
$k_\perp$ (cm^{-1})	13.1	13.8	8.9	9.7
$k_\parallel$ (cm^{-1})	0.15	0.20	0.04	0.07
k_r (cm^{-1}) [a]	−12.7	−13.4	−8.6	−9.4
$k_{\rm bi}$ (cm^{-1}) [b]	3.2	3.1	2.3	2.3
$k_{\rm tor}$ (cm^{-1}) [c]	1.4	1.4	1.1	1.1
$f_{\rm Dop}$ (MHz) [d]	1.78	1.64	1.35	1.26
$L_{\rm ol}$ (cm) [e]	20.6	19.2	30.0	27.7
$L_{\rm sv}$ (cm) [f]	2.8	2.8	4.2	4.2

[a]Wave vector component in the outward radial direction.
[b]Wave vector component in the ion diamagnetic direction.
[c]Wave vector component in the toroidal direction.
[d]Doppler shift due to toroidal rotation.
[e]Length of the overlap volume along the probe beam.
[f]Length of the scattering volume along the probe beam.

Core measurements at $r/a \simeq 0.15$ for discharge 124887 are shown in Fig. 7, but ion and electron drift directions are reversed from Fig. 5. Specifically, in Fig. 7, negative frequency corresponds to fluctuation wave vectors with a component in the electron diamagnetic direction, but toroidal rotation Doppler shifts spectral features to positive frequency (ion diamagnetic direction). Channel 4 in Fig. 7 corresponds to fluctuations with $k_\perp \rho_e \simeq 0.33$, and channel 5 corresponds to $k_\perp \rho_e \simeq 0.42$. The measurements demonstrate the existence of electron gyroscale fluctuations in the core of NSTX plasmas.

V. SUMMARY

A multichannel collective scattering system has been installed on NSTX to measure electron gyroscale fluctuations with spatial and k-space localization. Initial measurements indicate rich turbulent dynamics on the electron gyroscale in both core and outer regions of NSTX plasmas.

The system is configured for tangential scattering with probe and receiving beams nearly on the equatorial midplane. The system can measure fluctuations with $k_\perp \rho_e \lesssim 0.6$ and $k_\perp \lesssim 20$ cm^{-1}, and measured fluctuations are primarily radial. Steerable optics can position the scattering volume between the magnetic axis and the outboard edge. The large toroidal curvature of NSTX plasmas provides enhanced spatial localization by constricting the scattering volume within the beam overlap volume.

Electron thermal transport is anomalous in all NSTX confinement regimes, and ETG turbulence can be linearly unstable in NSTX plasmas. Ion thermal transport, on the other hand, is typically neoclassical in NSTX H-mode plasmas, and evidence suggests that ITG and TEM turbulences are suppressed by strong equilibrium $E \times B$ flow shear. The turbulence and transport properties of NSTX motivate efforts

to measure electron gyroscale fluctuations to investigate the connection between ETG turbulence and electron thermal transport. The NSTX collective scattering system is a vital tool for this investigation.

ACKNOWLEDGMENTS

This work was supported by the U.S. Department of Energy under Contract Nos. DE-AC02-76CH03073, DE-FG03-95ER54295, and DE-FG03-99ER54518.

[1] X. Garbet, P. Mantica, C. Angioni *et al.*, Plasma Phys. Controlled Fusion **46**, B557 (2004).
[2] W. Horton, Rev. Mod. Phys. **71**, 735 (1999).
[3] A. J. Wootton, B. A. Carreras, H. Matsumoto *et al.*, Phys. Fluids B **2**, 2879 (1990).
[4] W. Dorland, F. Jenko, M. Kotschenreuther, and B. N. Rogers, Phys. Rev. Lett. **85**, 5579 (2000).
[5] F. Jenko, W. Dorland, M. Kotschenreuther, and B. N. Rogers, Phys. Plasmas **7**, 1904 (2000).
[6] F. Jenko and W. Dorland, Phys. Plasmas **8**, 4096 (2001).
[7] F. Jenko and W. Dorland, Phys. Rev. Lett. **89**, 225001 (2002).
[8] W. M. Nevins, J. Candy, S. Cowley, *et al.*, Phys. Plasmas **13**, 122306 (2006).
[9] R. E. Waltz, J. Candy, and M. Fahey, Phys. Plasmas **14**, 056116 (2007).
[10] M. Ono, S. M. Kaye, Y.-K. M. Peng *et al.*, Nucl. Fusion **40**, 557 (2000).
[11] S. M. Kaye, M. G. Bell, R. E. Bell *et al.*, Phys. Plasmas **8**, 1977 (2001).
[12] B. P. LeBlanc, R. E. Bell, S. M. Kaye *et al.*, Nucl. Fusion **44**, 513 (2004).
[13] D. Stutman, M. Finkenthal, K. Tritz *et al.*, Phys. Plasmas **13**, 092511 (2006).
[14] S. M. Kaye, M. G. Bell, R. E. Bell *et al.*, Nucl. Fusion **46**, 848 (2006).
[15] F. M. Levinton, H. Yuh, M. G. Bell *et al.*, Phys. Plasmas **14**, 056119 (2007).
[16] S. M. Kaye, R. M. Levinton, D. Stutman *et al.*, Nucl. Fusion **47**, 499 (2007).
[17] S. M. Kaye, M. G. Bell, D. Gates *et al.*, Phys. Rev. Lett. **98**, 175002 (2007).
[18] D. R. Smith, E. Mazzucata, T. Munsat *et al.*, Rev. Sci. Instrum. **75**, 3840 (2004).
[19] W. Lee, H. K. Park, M H. Cho *et al.*, Rev. Sci. Instrum. **79**, 10E723 (2008).
[20] E. Mazzucato, Phys. Plasmas **10**, 753 (2003).
[21] E. Mazzucato, Plasma Phys. Controlled Fusion **48**, 1749 (2006).
[22] E. Mazzucato, Phys. Rev. Lett. **36**, 792 (1976).
[23] J. Sheffield, *Plasma Scattering of Electromagnetic Radiation* (Academic, New York, 1975).
[24] R. E. Slusher and C. M. Surko, Phys. Fluids **23**, 472 (1980).
[25] R. E. Bell, Rev. Sci. Instrum. **77**, 10E902 (2006).
[26] I. H. Hutchinson, *Principles of Plasma Diagnostics*, 2nd ed. (Cambridge University Press, Cambridge, UK, 2002).